ATMOSPHERIC SCIENCE

Periodic extreme rainfall in a warmer climate due to stronger convectively coupled waves

Heng Quan[1,2]*, Yi Zhang[3], Guy Dagan[4], Stephan Fueglistaler[1,2]

Tropical regions may experience periodic extreme precipitation and suffer from associated periodic deluges in a warmer climate. Recent studies conducted small-domain (around 100 kilometers by 100 kilometers) atmospheric model simulations and found that precipitation transitions from a steady state to a periodic oscillation state in a hothouse climate when the sea surface temperature reaches 320 to 325 kelvin. Here, we conduct global-scale atmospheric model simulations with varying complexity. We find that tropical precipitation in convective regions already transitions to a $\mathcal{O}$(10-day) periodic oscillation state with a $\mathcal{O}\left(100\ \text{mm}\ \text{day}^{-1}\right)$ amplitude at 305 to 310 kelvin, about 15 kelvin lower than previously reported and within reach in a century under a high–carbon emission scenario. Using a low-order analytical model, we attribute the onset of the periodic extreme precipitation to the intensification of convectively coupled waves that were not considered in the previous small-domain simulations. Our mechanism highlights the importance of the interaction between convection and atmospheric wave dynamics for climate change.

INTRODUCTION

Extreme precipitation events can cause severe economic loss and damage to natural systems (*1*), and they are projected to be more intense and frequent under global warming (*2*–*4*). Tropical regions, where the baseline precipitation is already high, are especially vulnerable to more severe extreme precipitation events in the future (*1*). In addition, projections of human population predict a continuing growth in countries in the tropics (20°S to 20°N) (*5*). Therefore, there is a pressing need to better understand the features and mechanisms of tropical extreme precipitation in a warmer climate down to regional scales.

Recent studies have found that tropical precipitation transitions to a periodic oscillation state in hothouse climates (*6*–*10*). These studies performed idealized small-domain (around 100 km by 100 km) simulations that explicitly resolve convection and found that precipitation only occurs in short outbursts (around 100 mm day^{-1}) lasting a few hours separated by multiday dry spells when the sea surface temperature (SST) reaches 320 to 325 K. This periodic extreme precipitation state would leave soils saturated, rivers swollen, and communities unable to recover before the next deluge strikes, resulting in a total damage far exceeding that of isolated extreme precipitation events of similar intensity. However, the critical SST is 20 to 25 K warmer than tropical SSTs in present climate. Such a hothouse climate state can be found in Earth's distant past with extremely high carbon dioxide levels (*11*–*13*) and potentially in the distant future with much larger solar insolation (*14*) but is unrealistic in the near future (*1*). Whether a similar transition can occur at lower, climatically relevant SSTs in more realistic global-scale simulations remains unknown.

Here, we report that global-scale simulations show a similar transition to periodic precipitation in a climate only 5 to 10 K warmer than present (where tropical SSTs reach 305 to 310 K). This SST threshold is much lower (about 15 K) than expected by previous work (320 to 325 K) based on small-domain simulations and may be reached in a century under high-emission scenarios according to model projections (*1*). We find that precipitation in tropical convective regions features a $\mathcal{O}$(10-day) periodic oscillation with a $\mathcal{O}\left(100\ \text{mm}\ \text{day}^{-1}\right)$ amplitude when the local SST reaches 305 to 310 K, resulting in severe periodic deluges. We attribute the transition to such a periodic precipitation state to the intensification of large-scale convectively coupled waves, which was not considered by previous work based on small-domain simulations. Our results demonstrate that the coupling between tropical waves and convection can substantially lower the temperature at which a transition to periodic extreme precipitation may be observed.

RESULTS

Global climate model projections

Figure 1 shows the response of tropical precipitation to global warming from global atmospheric model simulations with GFDL-AM4 (*15*, *16*) forced by SSTs in present climate and warmer climates. The GFDL-AM4 model has ~100-km horizontal resolution and parameterized convection. Figure 1 (A and B) shows that the spatial patterns of the climatological mean precipitation strengthen notably between 20°S and 20°N in a 10-K warmer climate, which is broadly consistent with the expected increase in precipitation over regions of convergence with increasing SSTs (*17*). In parallel, a transition from steady precipitation to periodic precipitation down to regional scales is evident in Fig. 1 (C to F), which shows the time series of 3-hourly precipitation in three climate states in four selected convective regions near the equator (red boxes in Fig. 1B). The regional-mean precipitation features small fluctuations about a steady mean state in the present climate (blue curves) but transitions to a $\mathcal{O}$(10-day) periodic oscillation with a $\mathcal{O}\left(100\ \text{mm}\ \text{day}^{-1}\right)$ amplitude in a 5- to 10-K warmer climate (black and red curves). While the increase in mean precipitation may be expected to project onto the amplitude of the oscillation, the power spectrum of the normalized precipitation by its regional mean (Fig. 1, G to J; see Materials and Methods) also shows that the spectral power of the $\mathcal{O}$(10-day) oscillation amplifies by a factor of 2 to 4 in a 5- to 10-K warmer climate. Consistent with the regional precipitation series in Fig. 1 (C to F), the spectral peaks in the +10-K simulations (red curves in Fig. 1, G to J)

[1]Department of Geosciences, Princeton University, Princeton, NJ, USA. [2]Program in Atmospheric and Oceanic Sciences, Princeton University, Princeton, NJ, USA. [3]Courant Institute of Mathematical Sciences, New York University, New York, NY, USA. [4]Institute of Earth Sciences, The Hebrew University of Jerusalem, Jerusalem, Israel.
*Corresponding author. Email: hengquan@princeton.edu

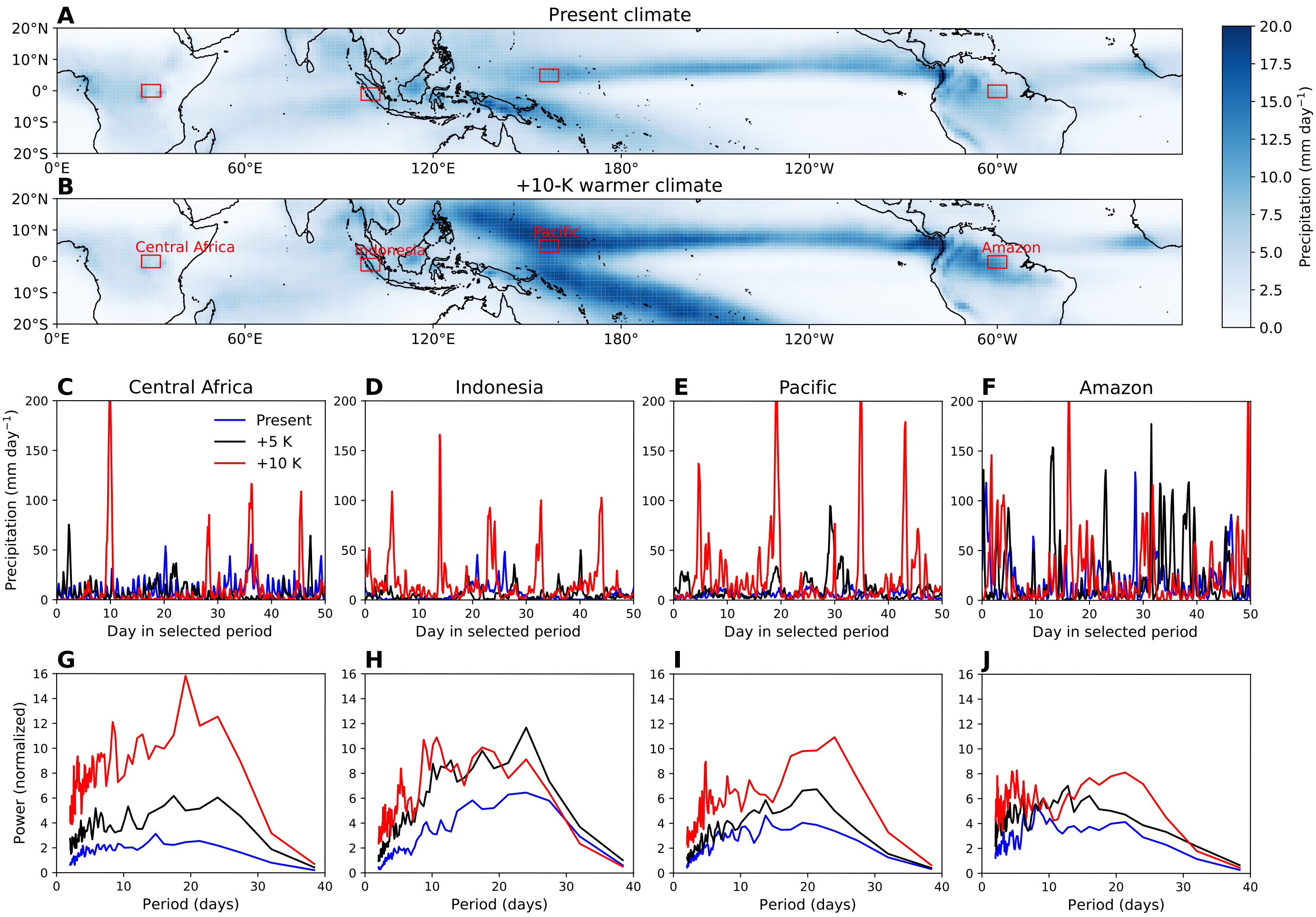

Fig. 1. Transition to periodic precipitation in global climate model simulations. (**A** and **B**) Tropical (20°S to 20°N) precipitation in present climate and a +10-K warmer climate. The results are averages over the last 10 years in 15-year simulations of the atmospheric model GFDL-AM4 (see Materials and Methods). (**C** to **F**) Regional mean 3-hourly precipitation time series in a selected 50-day period for four regions, in present climate (blue), a +5-K warmer climate (black) and a +10-K warmer climate (red). The results are from days 280 to 330 for Central Africa (3°S to 3°N, 26°E to 32°E), days 53 to 103 for Indonesia (4°S to 2°N, 95°E to 101°E), days 132 to 182 for Pacific (2°N to 8°N, 154°E to 160°E) and days 113 to 163 for Amazon (3°S to 3°N, 117°W to 123°E), all in the last simulation year. (**G** to **J**) The power spectra of the 3-hourly precipitation time series (normalized by the mean precipitation) over the last 10 years in different regions based on the Welch method (see Materials and Methods). A 32-day high-pass filter is used to remove intraseasonal and lower-frequency variability.

are close to 20 days in all regions except Indonesia, where the 10-day spectral power is slightly larger than 20-day.

Our targeted small-domain cloud-resolving model (CRM) simulations (Fig. 2A and movie S1) confirm the previously reported transition from steady precipitation to periodic precipitation with a $\mathcal{O}(100 \text{ mm day}^{-1})$ amplitude when the SST reaches 320 to 325 K (*6*–*10*). This transition has been explained to result from a net lower-tropospheric radiative heating due to the closing of the water vapor–infrared window regions (*6*). Subsequent studies reported that a large vertical gradient in radiative cooling rate—close to zero in lower troposphere but strong in upper troposphere—can also help to build up convective instability in the inhibition phase and trigger periodic precipitation (*8*, *7*). However, the transition to periodic precipitation in global climate model (GCM) simulations occurs at much lower SSTs around 305 to 310 K. In addition, the precipitation period is $\mathcal{O}(10 \text{ days})$ in GCM simulations (Fig. 1, C to J), which is much longer than the ~2- to 4-day precipitation period in the small-domain CRM simulations [Fig. 2A and (*6*, *8*)]. Although fig. S1 shows a larger vertical gradient of the radiative cooling rate with warming in GCM simulations that can help build up convective instability, fundamental differences in the SST threshold and the precipitation period imply different mechanisms responsible for the transition to periodic precipitation between global and small-domain simulations.

In the following, we argue that the transition to periodic precipitation in GCM simulations is instead related to the intensification of large-scale convectively coupled waves, which is not captured by the small-domain simulations in previous work. The tropical atmosphere sustains a group of convectively coupled wave modes (*18*, *19*) that control a substantial fraction of tropical precipitation variability (*20*, *21*). The GCM simulations shown in Fig. 1 exhibit an intensification of the eastward-propagating convectively coupled Kelvin waves under global warming, both in the Hovmoller diagrams of equatorial precipitation (i.e., the time-longitude plot; see fig. S2) and the equatorial wave spectra based on precipitation as well as outgoing longwave radiation (figs. S3 and S4). Despite the intensification

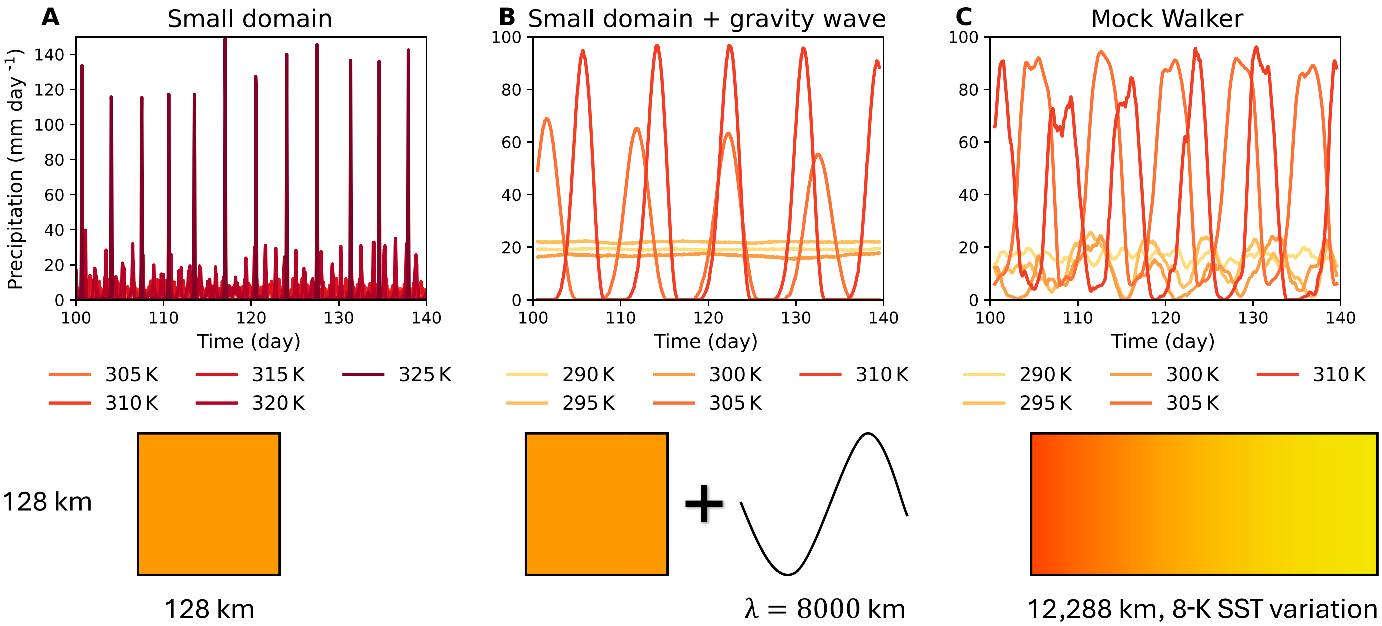

Fig. 2. Transition to periodic precipitation in CRM simulations. (**A**) Forty-day domain-mean precipitation time series in small-domain simulations, with the SST ranging from 305 to 325 K with an increment of +5 K. (**B**) Forty-day domain-mean precipitation time series in small-domain simulations coupled to gravity waves, with the SST ranging from 290 to 310 K with an increment of +5 K. (**C**) Forty-day precipitation time series averaged over the top 10% SSTs in 3D mock Walker simulations, with the domain-mean SST ranging from 290 to 310 K with an increment of +5 K.

of Kelvin waves, fig. S4 also indicates an increase in the phase speed (larger equivalent depth) with warming. These results from Geophysical Fluid Dynamics Laboratory (GFDL)–AM4 are consistent with the intensification and acceleration of Kelvin waves under global warming seen in almost all Coupled Model Intercomparison Project Phase 6 (CMIP6) GCMs (*22*). The intensification of a $\mathcal{O}$(10-day) Kelvin wave signal (fig. S3) is consistent with the $\mathcal{O}$(10-day) periodic precipitation in different regions in a 5- to 10-K warmer climate (Fig. 1, C to F), and the strongest Kelvin wave signal with a 20-day period (fig. S3C) is consistent with the spectral peak around 20 days in the precipitation power spectra in most regions (Fig. 1, G to J). This consistency implies that stronger convectively coupled waves are responsible for the transition to periodic precipitation with warming.

However, GCM simulations might have biases representing convectively coupled waves due to the coarse horizontal resolution [$\mathcal{O}$(100 km)] and convective parameterization (*23*–*25*). Therefore, we turn to more idealized large-scale cloud-resolving simulations with a much higher resolution (2 km) to demonstrate that convectively coupled waves will intensify and trigger periodic precipitation in a warmer climate.

CRM simulations

We use the CRM System for Atmospheric Modeling (SAM) (*26*) to study convectively coupled waves. We conduct mock Walker simulations (*27*) in a large domain (12,288 km by 128 km) with a horizontal resolution of 2 km (see Materials and Methods). These simulations have a linearly varying SST along the long, planetary-scale dimension, which mimics the east-west SST gradient across the equatorial Pacific and results in an overturning circulation similar to the Walker circulation in the tropical Pacific. These idealized simulations ignore subtropical forcings, topographic effects, and other complications in GCM simulations but capture the essential effects of convectively coupled waves as we will show below. We ignore the planetary rotation since it is weak close to the equator, so the mock Walker simulations only sustain convectively coupled gravity waves, which differs from the convectively coupled Kelvin waves in GCM simulations. However, studying the convectively coupled gravity waves in mock Walker simulations proves useful to understand the convectively coupled Kelvin waves in GCM simulations. As we will show below, they have the same propagation behavior and respond similarly to global warming, and both trigger periodic precipitation in a warmer climate because Kelvin waves and eastward-propagating gravity waves have the same dispersion relation $\omega = ck$ (where ω, c, and k represent frequency, phase speed, and wave number).

Figure 2C and movie S3 show the transition to periodic precipitation under global warming in mock Walker simulations. The 300-, 305-, and 310-K mock Walker simulations are comparable to the present, +5-K, and +10-K GCM simulations (Fig. 1, C to F), respectively. Convective regions in both models exhibit a transition to a $\mathcal{O}$(10-day) periodic precipitation with a $\mathcal{O}\left(100 \text{ mm day}^{-1}\right)$ amplitude in a 5- to 10-K warmer climate, whereas the small-domain simulations (Fig. 2A and movie S1) show the transition at the previously reported SST of 320 to 325 K. Mock Walker simulations with identical setup but a prescribed uniform radiative cooling rate ($Q_{\text{rad}} = -1.5 \text{ K day}^{-1}$) in the troposphere show the same transition (fig. S5), confirming that changes in radiative cooling are not the cause of the transition in our simulations. Instead, the intensification of large-scale convectively coupled gravity waves is evident when looking at the Hovmoller diagrams of precipitation (fig. S6). Figure S6 also shows that, in some simulations, gravity waves tend to have a single direction of propagation arising by chance (*8*, *27*), while in other simulations, gravity waves have both westward and eastward propagation with different phase speeds likely related to the background mean flow. In addition, we repeat the 310-K mock Walker simulation with the same SST (i.e., same phase speed of gravity waves) but varying domain sizes. Consistent with previous studies (*8*, *28*), fig. S7 shows that the precipitation period is equal to the travel time of convectively coupled gravity waves as they propagate away from and then return to the warm pool and, therefore, proportional to the length of the domain. These additional simulations further confirm the coupling between convection and gravity waves. Both the GCM simulations and the mock Walker simulations imply that convectively coupled waves play a central role in the transition to periodic precipitation.

To demonstrate that convectively coupled waves will intensify and trigger periodic precipitation in a warmer climate, we isolate their effects by running a new suite of cloud-resolving simulations, where we couple the small-domain simulations to large-scale gravity waves following (*29*) (see Materials and Methods). For simplicity, we assume that the large-scale gravity waves have a single horizontal wavelength of 8000 km, which is similar to the wavelength of Kelvin waves in GCM simulations (fig. S3) and comparable to the long dimension of the mock Walker simulations (12,288 km) but much larger than the size of the small dimension (128 km). As a result, the atmospheric motion in the entire small domain is largely synchronized by gravity waves. This type of wave-coupled simulation is a simplified representation of a locally convecting region such as the western Pacific warm pool and is not in radiative-convective equilibrium (RCE). Figure 2B and movie S2 show the time evolution of precipitation in the coupled simulations. When the SST is below 300 K, the coupled simulations are in steady states with precipitation larger than the corresponding RCE states, as discussed in (*30*). When the SST reaches 305 to 310 K, precipitation in the coupled simulations transitions to a $\mathcal{O}$(10-day) periodic oscillation state with a $\mathcal{O}\left(100 \text{ mm day}^{-1}\right)$ amplitude, consistent with the mock Walker simulations (Fig. 2C) and GCM simulations (Fig. 1, C to F). The transition to periodic precipitation is associated with the transition of the wave-induced vertical velocity from a perpetual ascending motion to a strong periodic oscillation between ascending and descending motion (fig. S8). The comparison between Fig. 2A and Fig. 2B indicates that large-scale convectively coupled waves alone can substantially lower the temperature for the transition to periodic precipitation. Therefore, we consider the coupled simulations in Fig. 2B as the minimum recipe to capture the transition to periodic precipitation in a warmer climate. In the following, we will analyze the coupled simulations to diagnose the mechanism behind the transition.

Mechanism of the transition

The periodic precipitation is related to the instability of convectively coupled waves. In a background RCE state, the potential temperature θ increases with height (Fig. 3A) while the specific humidity q decreases with height (Fig. 3B) in the troposphere. When a passing wave causes a domain-wise ascending motion and triggers convection in the lower troposphere, the vertical advection brings air with smaller θ and larger q upward, which cools and moistens the lower troposphere (Fig. 3C and Eqs. 6 and 7 in Materials and Methods). A colder temperature and a larger specific humidity both increase relative humidity and inhibit the evaporation of cloud condensates, which allows the convection to reach higher and results in more intense precipitation (*24*, *31*, *32*). This self-reinforcing process that amplifies convection competes against other self-limiting processes that terminate convection (for example, top-heavy latent heating from deep convection stabilizes the vertical stratification). If the self-reinforcing effect of wave-induced vertical advection dominates over other self-limiting processes for small perturbations relative to the RCE state, convectively coupled waves are unstable and precipitation features periodic oscillation.

The self-reinforcing effect of wave-induced vertical advection becomes more important with increasing SST. The vertical gradients of θ and q in the RCE state increase with warming (Fig. 3, A and B), which can be easily explained assuming a moist adiabat and a fixed relative humidity. As a result, the same wave-induced ascending velocity in the lower troposphere causes a larger advective cooling and moistening, so that the amplification of convection in Fig. 3C becomes stronger.

We hypothesize that the self-reinforcing effect of wave-induced vertical advection is weaker than other self-limiting processes when the SST is low, so convectively coupled waves are stable (weak) and precipitation is steady. By contrast, the self-reinforcing effect of wave-induced vertical advection becomes stronger and dominates over other self-limiting processes when the SST increases, so convectively coupled waves are unstable (strong) and precipitation features intense periodic oscillation. The SST threshold of the transition is around 305 K (Fig. 2B).

We verify our hypothesis using a low-order analytical model proposed in (*31*) (details summarized in Materials and Methods), which is a system of several ordinary differential equations (Eq. 15) that represents the coupling between convection and gravity waves. A standard stability analysis of the low-order model linearized around the RCE state indicates whether convectively coupled waves are stable under small perturbations: A positive maximum growth rate $\sigma > 0$ implies unstable waves and intense periodic oscillation in precipitation, while a negative maximum growth rate $\sigma < 0$ implies stable waves and steady precipitation. We extend on (*31*) by estimating the dependence of the model parameters on SST: c_1 (proportional to $|\mathrm{d}\theta/\mathrm{d}z|$) and a_1 (proportional to $|\mathrm{d}q/\mathrm{d}z|$) in the low-order model indicate the strength of the self-reinforcing effect of wave-induced vertical advection, and they increase with warmer SST (discussed above, more details in Materials and Methods). We calculate the maximum growth rate σ for different $\left(c_1, a_1\right)$ and show the contour plot in Fig. 3E, where a warmer SST corresponds to a move toward the upper-right corner in the $\left(c_1, a_1\right)$ phase space. We estimate the $\left(c_1, a_1\right)$ values corresponding to cloud-resolving simulations with different SSTs and plot five dots in the phase space. The maximum growth rate σ is negative for low SSTs but positive for high SSTs, and the transition occurs around 305 K, which is quantitatively consistent with the transition to periodic precipitation around 305 K in cloud-resolving simulations (Fig. 2B). Therefore, the low-order model verifies our hypothesis—the transition to periodic precipitation with warming is due to the destabilization (i.e., intensification) of convectively coupled waves, which is ultimately a result of larger vertical θ and q gradients in a warmer climate.

To further support the proposed mechanism, we run another group of simulations to isolate the effects of the vertical θ and q gradients. We take the 300-K simulation in Fig. 2B as the base simulation, which features stable convectively coupled waves and steady precipitation. We increase the vertical gradients of θ or q approximately to the corresponding values in the 310-K simulation only when calculating the wave-induced advective tendencies (Eqs. 6 and 7 in Materials and Methods), while fixing everything else including the SST to 300 K. According to the stability analysis of the low-order model, a

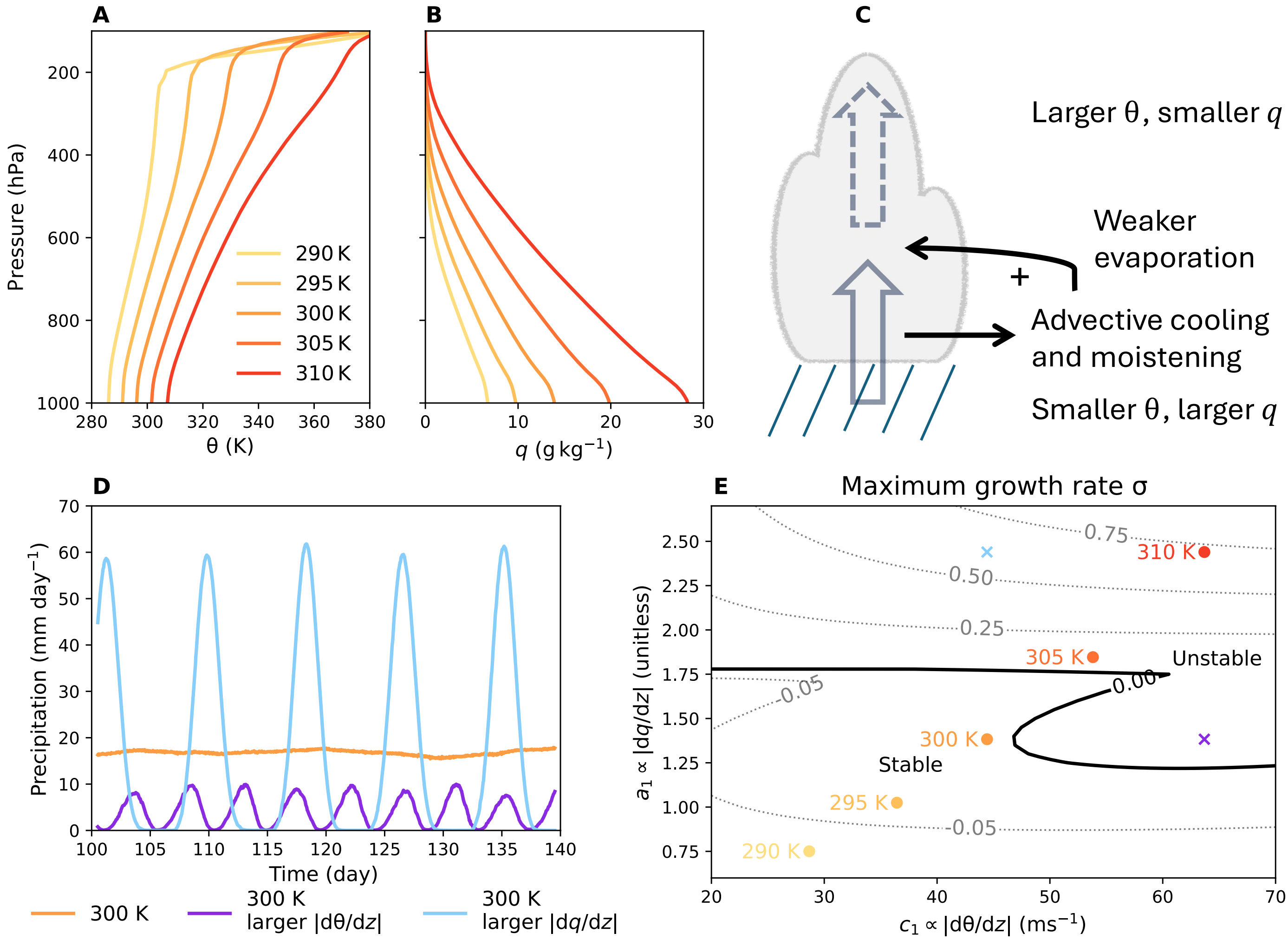

Fig. 3. The mechanism of the transition to periodic precipitation. (**A** and **B**) The steady-state (i.e., RCE) vertical profiles of domain-mean potential temperature θ and specific humidity q in small-domain cloud-resolving simulations, with the SST ranging from 290 to 310 K with an increment of +5 K. (**C**) A schematic showing how convectively coupled waves amplify convection. (**D**) Forty-day domain-mean precipitation time series in small-domain simulations coupled to gravity waves with the SST at 300 K (orange), the SST at 300 K but a larger vertical θ gradient (purple), and the SST at 300 K but a larger vertical q gradient (light blue). The perturbations to vertical θ and q gradients are only applied when calculating the wave-induced advective tendencies (Eqs. 6 and 7 in Materials and Methods). (**E**) The contour plot of the maximum growth rate σ as a function of parameters c_1 (proportional to $|d\theta/dz|$) and a_1 (proportional to $|dq/dz|$) from a low-order model (Eq. 15 in Materials and Methods). $\sigma > 0$ indicates instability and strong periodic precipitation. The positions of (c_1, a_1) corresponding to the five simulations coupled to gravity waves with varying SSTs (dots) and two 300-K perturbation simulations in (D) (crosses) are marked in the phase space.

larger $|d\theta/dz|$ (c_1) or $|dq/dz|$ (a_1) can both trigger instability, as $\sigma > 0$ for both the purple and light blue crosses in Fig. 3E. Consistent with the theoretical expectation, cloud-resolving simulations with a larger $|d\theta/dz|$ or $|dq/dz|$ both show periodic precipitation in Fig. 3D. The maximum growth rate σ in Fig. 3E is more sensitive to a_1 than to c_1, which is also consistent with Fig. 3D that a larger $|dq/dz|$ triggers a stronger periodic oscillation than a larger $|d\theta/dz|$. These results support our argument that the transition to periodic precipitation in a warmer climate is ultimately the result of larger vertical gradients of θ and q in the troposphere.

While we focus on the intensification of large-scale convectively coupled waves, there is another possibility that larger vertical gradients of θ and q might trigger periodic precipitation through negative gross moist stability [GMS (*33*); i.e., net energy import toward convecting regions—see Materials and Methods for details]. To test this possibility, we calculate the GMS for our small-domain cloud-resolving simulations coupled to gravity waves (Materials and Methods). Figure S9 indicates that the GMS is always positive and becomes larger with a warmer SST [consistent with (*34*, *35*)] or a larger vertical θ or q gradient alone, which means a more stabilizing effect. Therefore, the change in GMS with warming does not drive the transition to periodic precipitation, and the intensification of convectively coupled waves is more dominant.

Figure 4 (A to E) depicts the convection cycles in the 310-K small-domain simulation coupled to gravity waves. We divide each cycle into three phases: recharge, development, and decay. The recharge phase is a dry period with little or no precipitation (Fig. 4A), in which the large-scale passing wave causes a domain-wise descending motion in the lower troposphere (Fig. 4B). The vertical advection in the recharge phase thus warms (Fig. 4D) and dries (Fig. 4E) the lower troposphere, building up convective instability. The development phase features increasing precipitation (Fig. 4A), in which the unstable vertical stratification starts to trigger convection. The wave-induced domain-wise ascending motion in the development phase (Fig. 4B) cools (Fig. 4D) and moistens (Fig. 4E) the lower troposphere, inhibiting the evaporation of cloud condensates. This allows the convection to reach higher altitudes, resulting in latent heating of the upper troposphere by elevated condensation and latent cooling of the lower troposphere by evaporation of precipitation (Fig. 4C), which reinforces the temperature anomaly. Such a self-reinforcing process persists until the upper-tropospheric warming and lower-tropospheric cooling stabilize the vertical stratification and start to suppress convection, when the precipitation reaches the peak. After that, the precipitation decreases in the decay phase (Fig. 4A), and the convection cycle restarts from the recharge phase.

The convection cycles in the mock Walker simulations (fig. S10) are consistent with Fig. 4, confirming that the coupling between convection and large-scale atmospheric dynamics can be minimally represented by the coupling between convection and large-scale gravity waves with a single horizontal wave number. The convection cycles in the GCM simulations (Fig. 4, F to J) differ from Fig. 4 (A to E) in a longer period, a shorter time with intense precipitation, and a noisier vertical velocity structure. These differences are expected since the GCM sustains a group of waves with different wave numbers, whereas the CRM only sustains gravity waves with a single horizontal wave number. In addition, the GCM has complications like subtropical forcings and topographic effects, while the CRM assumes an idealized rectangular domain over the ocean. Nevertheless, the key self-reinforcing process in Fig. 3C—the lower-tropospheric cooling and moistening in the convection development phase—and the subsequent top-heavy latent heating are evident in both models. The Kelvin waves that are dominant in the GCM simulations (fig. S3) have the same dispersion relation ($\omega = ck$) as the (eastward-propagating) gravity waves in the cloud-resolving simulations, so they couple to

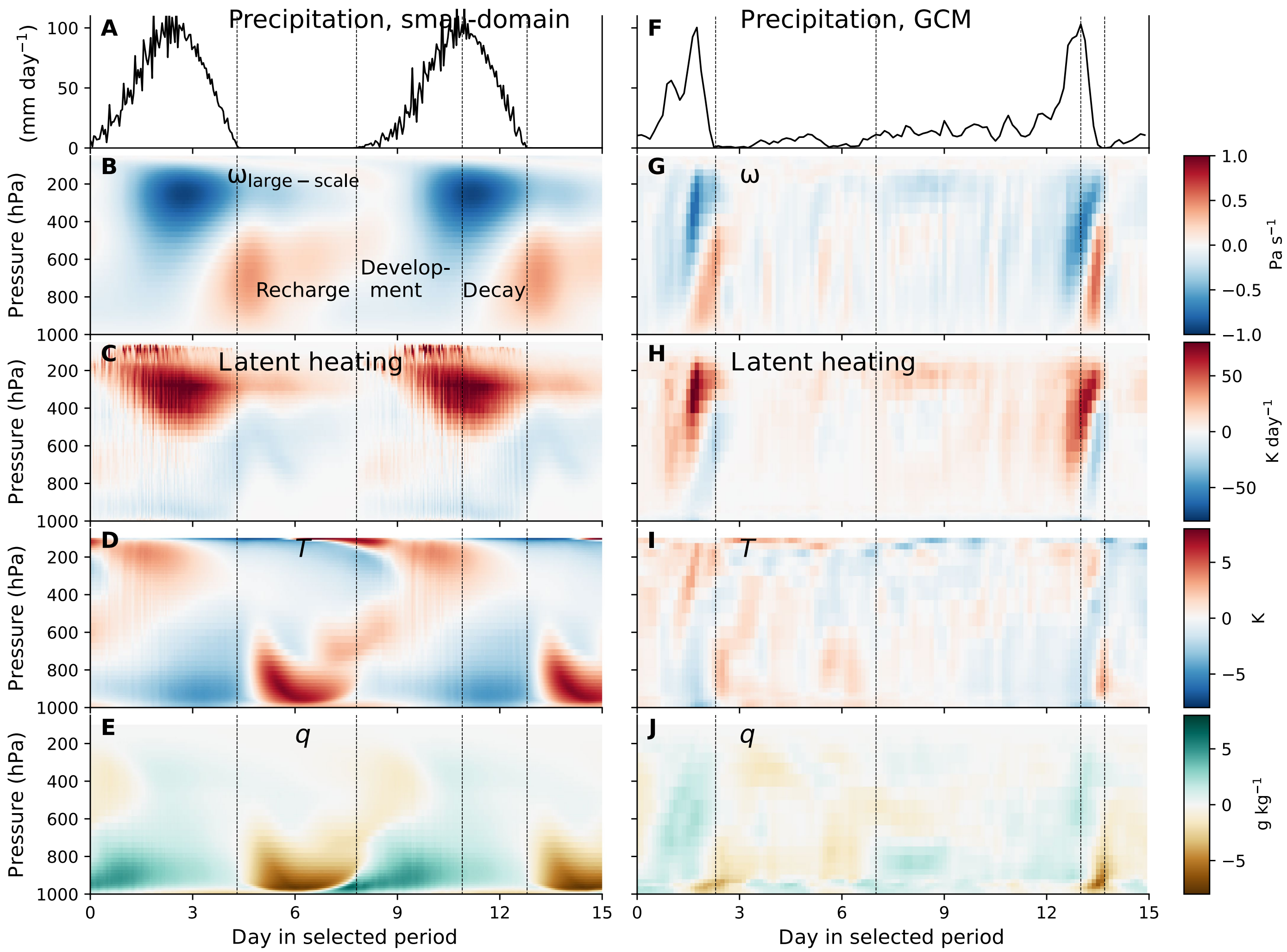

Fig. 4. The precipitation cycles in a warmer climate. The left column shows the 15-day time series of domain-mean variables from day 120 to day 135 of the 310-K small-domain cloud-resolving simulation coupled to gravity waves, and the right column shows the time series of the same variables averaged over the selected region in Indonesia from day 84 to day 99 in the last simulation year of the +10-K global climate model (GCM) simulation. (**A** and **F**) Precipitation. (**B** and **G**) Vertical velocity (induced by large-scale gravity waves for the left column). (**C** and **H**) Latent heating rate. (**D** and **I**) Temperature anomaly relative to the steady state. (**E** and **J**) Specific humidity anomaly relative to the steady state.

convection in the same way (*24*). Therefore, the two waves intensify similarly with increasing SST and trigger periodic precipitation, resulting in qualitatively consistent convection cycles in two models.

DISCUSSION

A few events similar to the periodic precipitation state described here have been reported in observations. For example, a periodic precipitation event associated with convectively coupled Kelvin waves was observed over the equatorial Indian Ocean in early November 2011 during the DYNAMO field campaign (*24*). Consistent with our theories, that event is explained by the self-reinforcement of convectively coupled waves (*24*), as depicted in Fig. 3C.

Our numerical simulations with different complexity and low-order analytical model all suggest that periodic precipitation will be more intense and frequent in convective regions in a 5- to 10-K warmer climate, which is much lower than previously reported. We attribute the transition to a $\mathcal{O}$(10-day) periodic precipitation with a $\mathcal{O}\left(100 \ \text{mm} \ \text{day}^{-1}\right)$ amplitude in a 5- to 10-K warmer climate to the intensification of convectively coupled waves, which is ultimately due to larger vertical θ and q gradients with increasing SST. The periodic precipitation state that we find is a temporal aggregation of convection, while previous studies documented the spatial aggregation of convection under global warming (*36*–*38*). Their interactions could be a direction for future work.

The time series of periodic precipitation in mock Walker simulations and small-domain cloud-resolving simulations coupled to gravity waves (Fig. 2, B and C) are quasi-sinusoidal, while the time series of periodic precipitation in global climate simulations (Fig. 1, C to J) are noisier. Despite this difference, all simulations feature a similar SST threshold (close to 305 K) for the transition to periodic extreme rainfall, a consistent $\mathcal{O}$(10-day) precipitation period and a consistent cycle of convectively coupled waves (Fig. 4), implying the same governing mechanism (Fig. 3) for different simulations. The difference in precipitation time series might result from real-world complications in GCM simulations that are not considered in idealized cloud-resolving simulations. The GCM simulations might have biases due to coarse resolution [$\mathcal{O}(100 \ \text{km})$] and convective parameterization (*23*–*25*), while the CRM simulations only consider the equatorial Pacific and only sustain gravity waves. Future work may run global CRM simulations with kilometer-scale resolution to more accurately study the coupling between convection and large-scale waves. The results presented here emphasize the importance of the coupling between convection and atmospheric wave dynamics and point to the need to include these interactions also in "idealized" model configurations to capture regime transitions under global warming.

MATERIALS AND METHODS

GCM simulations

We use the GFDL atmospheric general circulation model AM4 (*15*, *16*) to conduct global atmospheric simulations. AM4 uses a horizontal grid spacing of ∼100 km and saves the data to disk on a grid with 180 grid points in the meridional and 288 grid points in the zonal direction (i.e., 1.0° × 1.25° for the horizontal resolution). The greenhouse gas concentrations and aerosol emissions correspond to the conditions of the year 2000 in all simulations. The control simulation ("present climate") is forced by the observed climatological (1982 to 2001) monthly means of SSTs and sea ice concentrations from the HADISST1 dataset (*39*), and the zonal SST profile in the equatorial Pacific region is similar to the 300-K mock Walker simulation. We have a uniform SST + 5-K simulation and a uniform SST + 10-K simulation, comparable to the 305- and 310-K mock Walker simulations, respectively. All AM4 simulations are integrated for 15 years, with the first 5 years discarded to eliminate spin-up effects. All our results are based on the last 10 years of 3-hourly model output.

Computing the power spectrum of the precipitation time series

We compute the power spectrum of the 3-hourly precipitation time series in selected regions over the last 10 years of the GCM simulations using the Welch method. We first normalize the raw series (i.e., divide the raw series by the time-average precipitation) so that the change of the power spectrum is independent of the change in time-average precipitation with warming. Then, we remove the mean from the normalized series and apply a zero-phase, fourth-order high-pass Butterworth filter with a 32-day cutoff period to the series to remove intraseasonal and lower-frequency variability (e.g., Madden-Julian Oscillation). After that, we divide the full series into 192-day segments with 128-day overlaps and calculate the spectrum power (squared modulus of the spectrum) for each segment using Fourier transform with a Hann window. The final spectrum is obtained by averaging over all segments, which reduces sampling variability relative to a single spectrum while preserving robust spectral peaks. Sensitivity tests using a cutoff period from 25 to 50 days and segment lengths from 160 to 240 days yield consistent results.

We assess the statistical significance of the difference between two spectra using a band-averaged F test. We first average the power spectra over the 5- to 25-day band and compare the band-mean power ratio between two spectra against an F distribution with degrees of freedom determined by the number of independent Welch segments and frequency bins. According to a one-sided test, the normalized precipitation series has a significantly larger power ($P < 0.01$) over the 5- to 25-day band for a 5-K SST increase (both 300 to 305 K and 305 to 310 K) in all selected regions.

Computing the equatorial wave spectrum

We compute the equatorial (10°S to 10°N) wave spectrum from the GCM output according to the method in (*20*). We first remove the first three harmonics of the seasonal cycle (with 1-, 1/2-, and 1/3-year period) from the raw output to filter out low-frequency signals. Because linear equatorial waves are either symmetric or antisymmetric about the equator, we decompose any given variable into a symmetric component $FS(\varphi) = \frac{F(\varphi) + F(-\varphi)}{2}$ and an antisymmetric component $FA(\varphi) = \frac{F(\varphi) - F(-\varphi)}{2}$, where φ is the latitude. Then, we partition the time series of each component into 96-day segments, overlapping by 64 days. We remove the mean and linear trend from each segment and apply two-dimensional (2D) discrete Fourier transforms in time and zonal directions. We average the spectrum power, i.e., squared modulus of the spectrum, over all segments and all latitudes. To get the background spectrum featuring red noise, we apply a 1-2-1 filter 40 times in the frequency dimension and 10 times in the wave number dimension to the raw spectrum. We calculate the significance level by taking the ratio of the raw power spectrum to the smoothed background spectrum. A higher ratio means a stronger wave signal, and the 95% significance level of the ratio is 1.162 according to a chi-square test.

Cloud-resolving simulations

We use SAM (*26*) version 6.11.5 CRM. The model is nonhydrostatic, uses one-moment bulk microphysics and a simple Smagorinsky-type scheme for subgrid turbulence, and computes the surface sensible heat, latent heat, and momentum fluxes based on the Monin-Obukhov similarity theory. All simulations use a CO_2 concentration of 355 parts per million (ppm), and the concentrations of other trace gases are set to the default values. The SST is prescribed in all cloud-resolving simulations.

Most simulations (except those with the SST warmer than 310 K) have a vertical grid of 64 levels, starting at 25 m and extending up to 27 km, and the vertical grid spacing increases from 50 m at the lowest levels to roughly 1 km at the top of the domain. The model has a rigid lid at the top with a wave-absorbing layer occupying the upper third of the domain to prevent the reflection of gravity waves. The domain size is varied over a wide range of sizes and geometries, and the horizontal resolution is 2 km.

A time step of 5 s is used. Radiative fluxes are calculated every 5 min using the CAM (Community Atmosphere Model) radiation scheme (*40*), except for experiments using prescribed radiative cooling rates. Following (*41*), the incoming solar radiation is fixed at 650.83 W m^{-2}. Small temperature perturbations are added near the surface at the beginning of the simulation to initialize convection. All simulations are run for 140 days and reach equilibrium after $\sim$50 days. All our results are based on the last 40 days of hourly model output.

We run two types of CRM simulations—small-domain simulations resolving convective-scale dynamics and mock Walker simulations (*27*) resolving both convective-scale dynamics and its interaction with large-scale dynamics. They are summarized in table S1.

For small-domain simulations, the domain size is 128 km by 128 km, and we use doubly periodic boundary conditions. The SST is uniform and ranging from 290 to 325 K with an increment of +5 K. The vertical grid is composed of 81 levels, which follows the Radiative–Convective Equilibrium Model Intercomparison Project (RCEMIP) protocol (*42*) up to a height of 33 km and is extended to 40 km with 1-km resolution to account for the deeper troposphere under higher SSTs. We have another group of small-domain simulations coupled to gravity waves [(*29*), more details below] with the SST ranging from 290 to 310 K with an increment of +5 K. We have two perturbation simulations based on the coupled 300-K simulation: one with the vertical q gradient multiplied by a factor of 1.8 only when calculating the wave-induced advective q tendency [$\left(\frac{\partial q}{\partial t}\right)_{\text{large-scale}}$ in Eq. 7], the other with the vertical θ gradient multiplied by a factor of 1.4 only when calculating the wave-induced advective T tendency [$\left(\frac{\partial T}{\partial t}\right)_{\text{large-scale}}$ in Eq. 6]. The factors 1.8 and 1.4 are the ratios of the parameters a_1 and c_1 (more details below) between the 310-K simulation and the 300-K simulation in our low-order model, as shown in Fig. 3E.

For mock Walker simulations, the domain size is $12,288$ km by 128 km for 3D simulations and $12,288$ km for 2D simulations. We use solid-wall boundary conditions at the two edges in the long dimension and periodic boundary conditions in the short dimension (for 3D runs). Following (*43*), the SSTs linearly decrease by 8 K from the left boundary ($x = 0$) to the right boundary ($x = 12,288$ km), mimicking the east-west SST gradient across the equatorial Pacific and causing an overturning circulation. The domain average SST ranges from 290 to 310 K with an increment of +5 K. We have two more 2D 310-K mock Walker simulations with smaller domain size $L/2 = 6144$ km and $L/3 = 4096$ km, and they also have an 8-K SST contrast between two edges. We have another group of 2D mock Walker simulations with the interactive radiative transfer disabled by prescribing a uniform radiative cooling rate $Q_{\text{rad}} = -1.5$ K day^{-1} throughout the troposphere (where the temperature is warmer than 207.5 K) and using a Newtonian relaxation toward 200 K in the stratosphere ("fixed QRAD" in table S1) (*44*).

Coupling gravity waves to small-domain CRM simulations

We use the method from (*29*) to parameterize gravity waves in small-domain CRM simulations and study the interaction between convection and large-scale dynamics. We start by considering the linearized large-scale wave equations in a nonrotating 2D anelastic system

$$\frac{\partial u'}{\partial t} = -\frac{\partial \phi'}{\partial x} - \varepsilon u' \tag{1}$$

$$\frac{\partial u'}{\partial x} + \frac{\partial \omega'}{\partial p} = 0 \tag{2}$$

$$\frac{\partial \phi'}{\partial p} = -\frac{R_d T'}{p} \tag{3}$$

These equations are the perturbation equations of momentum, continuity, and hydrostatic balance. ε is the momentum damping coefficient, and other symbols assume their standard meteorological meaning. The virtual effect is negligible in this system (*29*, *30*), so we use temperature instead of virtual temperature in Eq. 3. We assume u', w', T', ϕ' have a single horizontal wave number $k = \frac{2\pi}{\lambda}$, so that $\frac{\partial}{\partial x} = ik$. After eliminating u' and ϕ' from Eqs. 1 to 3, we have

$$\left(\frac{\partial}{\partial t} + \varepsilon\right)\frac{\partial^2 \omega'}{\partial p^2} = k^2 \frac{R_d T'}{p} \tag{4}$$

Because the dimension of the small-domain simulations [$\mathcal{O}(100$ km$)$] is much smaller than the wavelength of the gravity waves that we consider [$\mathcal{O}(10,000$ km$)$, the long dimension of the mock Walker runs), we interpret w' as the spatially uniform vertical velocity induced by large-scale gravity waves, i.e., $\omega_{\text{large-scale}}$. Similarly, T' is interpreted as the deviation of the domain-average temperature from a reference RCE state, $\langle T \rangle - T_{\text{RCE}}$. Therefore, we have

$$\left(\frac{\partial}{\partial t} + \varepsilon\right)\frac{\partial^2 \omega_{\text{large-scale}}}{\partial p^2} = k^2 \frac{R_d\left(\langle T \rangle - T_{\text{RCE}}\right)}{p} \tag{5}$$

The vertical velocity due to large-scale gravity waves advects temperature and moisture in the small-domain, so the tendency equations of temperature and specific humidity are written as

$$\frac{\partial T}{\partial t} = S_T \underbrace{- \omega_{\text{large-scale}}\left(\frac{p}{p_0}\right)^{\frac{R_d}{c_p}} \frac{d\theta_{\text{RCE}}}{dp}}_{\left(\frac{\partial T}{\partial t}\right)_{\text{large-scale}}} \tag{6}$$

$$\frac{\partial q}{\partial t} = S_q \underbrace{- \omega_{\text{large-scale}} \frac{dq_{\text{RCE}}}{dp}}_{\left(\frac{\partial q}{\partial t}\right)_{\text{large-scale}}} \tag{7}$$

The source terms S_T and S_q are convective-scale tendencies simulated explicitly by the model, and we add the terms $\left(\frac{\partial T}{\partial t}\right)_{\text{large-scale}}$ and $\left(\frac{\partial q}{\partial t}\right)_{\text{large-scale}}$ to represent the effects of large-scale gravity waves. The resulting temperature is used in Eq. 5 to diagnose $\omega_{\text{large-scale}}$ for the next time step.

The reference RCE profiles T_{RCE}, θ_{RCE}, and q_{RCE} are obtained by averaging the corresponding variables over the last 40 days of the small-domain simulations without gravity wave coupling, and they are the initial conditions of the small-domain simulations coupled to gravity waves. We use $\varepsilon = 0.25\ \text{day}^{-1}$ and $\lambda = 8000$ km in all simulations. A different choice might affect the exact critical SST for the transition to periodic convection, but the transition still occurs as the SST warms.

A low-order analytical model for the transition

A previous research (*31*) developed a low-order analytical model of two vertical modes to explain the periodic precipitation (instability) in small-domain CRM simulations coupled with large-scale gravity waves. Here, we use that model to explain the transition from steady precipitation (stable) to periodic precipitation (unstable) with increasing SST in our CRM simulations (Fig. 2B). Below, we briefly describe the model, and readers interested in details are encouraged to refer to (*31*).

The low-order model is based on Eqs. 6 and 7. To be consistent with the notation in (*31*), we first rewrite these three equations in z-coordinate

$$\left(\frac{\partial}{\partial t}+\varepsilon\right)\frac{\partial^2}{\partial z^2}\left(\rho_{\text{RCE}}\ w_{\text{large-scale}}\right)=-k^2\rho_{\text{RCE}}\ g\frac{\langle T\rangle-T_{\text{RCE}}}{T_{\text{RCE}}} \quad (8)$$

$$\frac{\partial T}{\partial t}=S_T-w_{\text{large-scale}}\left(\frac{p}{p_0}\right)^{\frac{R_d}{c_p}}\frac{\mathrm{d}\theta_{\text{RCE}}}{\mathrm{d}z} \quad (9)$$

$$\frac{\partial q}{\partial t}=S_q-w_{\text{large-scale}}\frac{\mathrm{d}q_{\text{RCE}}}{\mathrm{d}z} \quad (10)$$

The low-order model reduces the partial differential equations to a group of ordinary differential equations by vertical-mode decomposition. For vertical velocity, (domain-mean) temperature, and convective heating rate, it only considers the first and second baroclinic modes,

$$\begin{aligned}\rho_{\text{RCE}}(z)w_{\text{large-scale}}(t,z)&=\sum_{j=1}^{2}w_j(t)G_j(z)\\ \rho_{\text{RCE}}(z)\ [\langle T\rangle(t,z)-T_{\text{RCE}}(z)]&=\sum_{j=1}^{2}T_j(t)G_j(z)\left(\frac{p}{p_0}\right)^{\frac{R_d}{c_p}}\frac{\mathrm{d}\theta_{\text{RCE}}}{\mathrm{d}z}\\ \rho_{\text{RCE}}(z)\ \langle S_T\rangle(t,z)&=\sum_{j=1}^{2}J_j(t)G_j(z)\left(\frac{p}{p_0}\right)^{\frac{R_d}{c_p}}\frac{\mathrm{d}\theta_{\text{RCE}}}{\mathrm{d}z}\end{aligned} \quad (11)$$

so that Eqs. 8 and 9 become four linear prognostic equations for w_1, w_2, T_1, and T_2

$$\begin{aligned}\left(\frac{\mathrm{d}}{\mathrm{d}t}+\varepsilon\right)w_j-k^2c_j^2T_j&=0\\ \frac{\mathrm{d}}{\mathrm{d}t}T_j+w_j&=J_j\end{aligned} \quad (12)$$

If we assume a vertically constant stratification (square of buoyancy frequency, $N^2=\frac{g}{\theta_{\text{RCE}}}\frac{\mathrm{d}\theta_{\text{RCE}}}{\mathrm{d}z}S_j$), the vertical mode takes the simple form $G_j(z)=\frac{\pi}{2}\sin\frac{j\pi z}{H}$, with the corresponding dry phase speed $c_j=\frac{NH}{j\pi}$ where H is the depth of the troposphere.

For moisture, the low-order model only considers the ~600-hPa (domain-mean) specific humidity q, which substantially affects the strength of entrainment evaporation. Therefore, Eq. 10 becomes a single linear prognostic equation for q, in which the (domain-mean) convective moisture tendency $\langle S_q\rangle$ is expressed as a linear combination of J_1 and J_2

$$\frac{\mathrm{d}q}{\mathrm{d}t}=a_1w_1+a_2w_2-d_1J_1-d_2J_2 \quad (13)$$

where a_1 is proportional to the vertical q_{RCE} gradient and $a_2\approx 0$ because $G_2\approx 0$ at 600 hPa.

The system will be closed with an additional convective parameterization—once the tendencies of J_1 and J_2 are expressed in terms of w_j, T_j, q, and J_j. The model assumes that J_1 and J_2 are not independent, because the ratio between the upper-tropospheric convective heating $U=(J_1-J_2)/2$ and the lower-tropospheric convective heating $L=(J_1+J_2)/2$ can be related to q and T_1: A moister or colder mid-troposphere means a smaller saturation deficit, a weaker entrainment evaporation, hence a deeper convection and a larger U/L ratio. Therefore, J_1 and J_2 can be expressed in terms of L, q, and T_1.

The model further assumes that the lower tropospheric convective heating L is relaxed toward an equilibrium value L_{eq}

$$\frac{\partial L}{\partial t}=\frac{L_{\text{eq}}-L}{\tau_L} \quad (14)$$

where L_{eq}, expressed in terms of T_1, q, w_1, and w_2, is the lower tropospheric convective heating rate required to maintain the subcloud-layer moist static energy in strict quasi-equilibrium with the saturation moist static energy above the cloud base.

After linearizing the dependence of U/L on T_1 and q around the RCE state, we get six linear prognostic equations, Eqs. 12 to 14, for six variables w_1, w_2, T_1, T_2, q, and L (all representing perturbations relative to the RCE state). We write the six equations together and get the following governing equation

$$\frac{\mathrm{d}}{\mathrm{d}t}\begin{pmatrix}w_1\\ w_2\\ T_1\\ T_2\\ q\\ L\end{pmatrix}=\begin{pmatrix}-\varepsilon & 0 & k^2c_1^2 & 0 & 0 & 0\\ 0 & -\varepsilon & 0 & k^2c_2^2 & 0 & 0\\ -1 & 0 & -\frac{3r_q}{2} & 0 & r_q & 1+r_0\\ 0 & -1 & \frac{3r_q}{2} & 0 & -r_q & 1-r_0\\ a_1 & a_2 & \frac{3r_q(d_1-d_2)}{2} & 0 & -r_q(d_1-d_2) & -d_1(1+r_0)-d_2(1-r_0)\\ \frac{f}{\tau_LB} & \frac{1-f}{\tau_LB} & -\frac{3Ar_q}{2\tau_LB} & 0 & \frac{Ar_q}{\tau_LB} & -\frac{1}{\tau_L}\end{pmatrix}\begin{pmatrix}w_1\\ w_2\\ T_1\\ T_2\\ q\\ L\end{pmatrix} \quad (15)$$

where we express T_j and q (by multiplying a factor of L_v/c_p) in temperature unit (1 K) while w_j and L in 1 K day^{-1} following the normalization in (*31*). All dimensional parameters are nondimensionalized by $T=1$ day, $L=4320$ km, and $U=50$ ms^{-1}. We define the maximum growth rate σ as the maximum real part among all eigenvalues of the matrix in Eq. 15. $\sigma>0$ indicates that the linearized system is unstable to small perturbations relative to the RCE state, and there is likely intense periodic precipitation in the corresponding CRM simulation.

We extend on (*31*) by considering the dependence of two important parameters of the low-order model, a_1 and c_1, on the underlying SST. We estimate the values of a_1 and c_1 corresponding to our small-domain CRM simulations with varying SSTs.

1. $c_1 = \frac{NH}{\pi}$ if the stratification $N^2 = \frac{g}{\theta_{\mathrm{RCE}}}\frac{d\theta_{\mathrm{RCE}}}{dz}$ is vertically constant. With a warmer SST, N increases (around 1.5%/K) and the depth of the troposphere H also increases (around 1.5%/K), so c_1 increases. For simplicity, we estimate the tropospheric average stratification and tropospheric depth in small-domain CRM simulations with different SSTs and use them to estimate the dry phase speed c_1 for different SSTs.

2. $a_1 \propto \frac{dq_{\mathrm{RCE}}}{dz} \sim \frac{q_{\mathrm{RCE},s}}{H}$, where $q_{\mathrm{RCE},s}$ means the surface specific humidity in the RCE state. With a warmer SST, $q_{\mathrm{RCE},s}$ increases according to the Clausius-Clapeyron scaling (around 7%/K), which is much larger than the increase in H (around 1.5%/K). Therefore, we assume that a_1 also increases with SST at 7%/K. The previous literature (*31*) estimated that $a_1 = 1.6$ from a 302.5-K simulation, so we estimate a_1 for other SSTs taking this as the reference.

We assume that other parameters (except $c_2 = c_1/2$) do not change with SST. We use $\varepsilon = 0.25\ \mathrm{day}^{-1}$ and $k = 2\pi/\lambda$ where $\lambda = 8000\ \mathrm{km}$. The values of other parameters follow those in (*31*) (see its Appendix A) and are listed in table S2. The analytical model successfully reproduces the transition to periodic precipitation (instability) with increasing SST seen in CRM simulations coupled to gravity waves (Fig. 3E), which indicates that scaling a_1 and c_1 with SST is sufficient for the model to reproduce the transition; however, the role of other processes is not assessed here, as there is no clear theoretical basis for how they should vary with SST.

In Fig. 3D, we have two perturbation simulations based on the 300-K simulation coupled to gravity waves: one with $\frac{dq_{\mathrm{RCE}}}{dz}$ in Eq. 10 multiplied by a factor of 1.8, the other with $\frac{d\theta_{\mathrm{RCE}}}{dz}$ in Eq. 9 multiplied by a factor of 1.4, so that the parameters a_1 and c_1 become that corresponding to the 310-K simulation according to our analytical model.

Calculating the GMS in small-domain cloud-resolving simulations coupled to gravity waves

The GMS measures the efficiency with which a convective atmospheric column exports energy and indicates whether convection is stabilized or destabilized (*33*). The GMS has many definitions (*45*). For our small-domain cloud-resolving simulations coupled to gravity waves, we use a definition similar to (*34*, *46*)

$$\mathrm{GMS} = -\frac{\int_{p_t}^{p_s} \omega_{\mathrm{large-scale}} \frac{d\mathrm{MSE}}{dp}\, dp}{\omega^*_{\mathrm{large-scale}}} \tag{16}$$

where $\omega_{\mathrm{large-scale}}(p)$ is the time-averaged large-scale wave-induced vertical velocity, $\mathrm{MSE}(p) = c_p T + L_v q + gz$ is the moist static energy averaged in space and time, and $\omega^*_{\mathrm{large-scale}}$ is the peak ascending velocity of $\omega_{\mathrm{large-scale}}(p)$ (usually in the mid-troposphere). p_s is the surface pressure, and p_t is the pressure at the tropopause defined as the level with the minimum temperature. A positive GMS means convection exports energy (stabilizing), while a negative GMS means convection imports energy (destabilizing).

In fig. S9, we show $\omega_{\mathrm{large-scale}}(p)$, $\mathrm{MSE}(p)$, and GMS in Eq. 16 for small-domain cloud-resolving simulations coupled to large-scale gravity waves with SSTs varying from 290 to 310 K, the 300-K simulation with a larger vertical θ gradient, and the 300-K simulation with a larger vertical q gradient. The GMS is always positive and becomes larger with a warmer SST or a larger θ or q gradient, indicating that the change in GMS does not drive the transition to periodic precipitation.

Supplementary Materials

The PDF file includes:
Figs. S1 to S10
Tables S1 and S2
Legends for movies S1 to S3

Other Supplementary Material for this manuscript includes the following:
Movies S1 to S3

REFERENCES

1. H. Lee, K. Calvin, D. Dasgupta, G. Krinner, A. Mukherji, P. Thorne, C. Trisos, J. Romero, P. Aldunce, K. Barrett, G. Blanco, W. W. L. Cheung, S. L. Connors, F. Denton, A. Diongue-Niang, D. Dodman, M. Garschagen, O. Geden, B. Hayward, C. Jones, F. Jotzo, T. Krug, R. Lasco, J.-Y. Lee, V. Masson-Delmotte, M. Meinshausen, K. Mintenbeck, A. Mokssit, F. E. L. Otto, M. Pathak, A. Pirani, E. Poloczanska, H.-O. Pörtner, A. Revi, D. C. Roberts, J. Roy, A. C. Ruane, J. Skea, P. R. Shukla, R. Slade, A. Slangen, Y. Sokona, A. A. Sörensson, M. Tignor, D. van Vuuren, Y.-M. Wei, H. Winkler, P. Zhai, Z. Zommers, J. Romero, J. Kim, E. F. Haites, Y. Jung, R. Stavins, A. Birt, M. Ha, D. J. A. Orendain, L. Ignon, S. Park, Y. Park, Intergovernmental Panel on Climate Change (IPCC), *Climate Change 2022 – Impacts, Adaptation and Vulnerability: Working Group II Contribution to the Sixth Assessment Report of the Intergovernmental Panel on Climate Change* (Cambridge Univ. Press, 2023).
2. S.-K. Min, X. Zhang, F. W. Zwiers, G. C. Hegerl, Human contribution to more-intense precipitation extremes. *Nature* **470**, 378–381 (2011).
3. J. Lehmann, D. Coumou, K. Frieler, Increased record-breaking precipitation events under global warming. *Clim. Change* **132**, 501–515 (2015).
4. S. B. Guerreiro, H. J. Fowler, R. Barbero, S. Westra, G. Lenderink, S. Blenkinsop, E. Lewis, X.-F. Li, Detection of continental-scale intensification of hourly rainfall extremes. *Nat. Clim. Change* **8**, 803–807 (2018).
5. S. Legg, World population prospects 2024: Summary of results. *Interaction* **52**, 18–25 (2024).
6. J. T. Seeley, R. D. Wordsworth, Episodic deluges in simulated hothouse climates. *Nature* **599**, 74–79 (2021).
7. X. Song, D. S. Abbot, J. Yang, Critical role of vertical radiative cooling contrast in triggering episodic deluges in small-domain hothouse climates. *J. Adv. Model. Earth Syst.* **16**, e2023MS003912 (2024).
8. G. Dagan, J. T. Seeley, N. Steiger, Convection and convective-organization in hothouse climates. *J. Adv. Model. Earth Syst.* **15**, e2023MS003765 (2023).
9. F. E. Spaulding-Astudillo, J. L. Mitchell, A simple model for the emergence of relaxation-oscillator convection. *J. Adv. Model. Earth Syst.* **16**, e2024MS004439 (2024).
10. D. Yang, D. S. Abbot, S. Seidel, Predator and prey: A minimum recipe for the transition from steady to oscillating precipitation in hothouse climates. arXiv:2408.11350 [physics.ao-ph] (2024).
11. N. H. Sleep, The Hadean-Archaean environment. *Cold Spring Harb. Perspect. Biol.* **2**, a002527 (2010).
12. B. Charnay, G. Le Hir, F. Fluteau, F. Forget, D. C. Catling, A warm or a cold early Earth? New insights from a 3-D climate-carbon model. *Earth Planet. Sci. Lett.* **474**, 97–109 (2017).
13. R. Pierrehumbert, D. S. Abbot, A. Voigt, D. Koll, Climate of the Neoproterozoic. *Annu. Rev. Earth Planet. Sci.* **39**, 417–460 (2011).
14. C. Goldblatt, A. J. Watson, The runaway greenhouse: Implications for future climate change, geoengineering and planetary atmospheres. *Phil. Trans. R. Soc. A* **370**, 4197–4216 (2012).
15. M. Zhao, J.-C. Golaz, I. M. Held, H. Guo, V. Balaji, R. Benson, J.-H. Chen, X. Chen, L. J. Donner, J. P. Dunne, K. Dunne, J. Durachta, S.-M. Fan, S. M. Freidenreich, S. T. Garner, P. Ginoux, L. M. Harris, L. W. Horowitz, J. P. Krasting, A. R. Langenhorst, Z. Liang, P. Lin, S.-J. Lin, S. L. Malyshev, E. Mason, P. C. D. Milly, Y. Ming, V. Naik, F. Paulot, D. Paynter, P. Phillipps, A. Radhakrishnan, V. Ramaswamy, T. Robinson, D. Schwarzkopf, C. J. Seman, E. Shevliakova, Z. Shen, H. Shin, L. G. Silvers, J. R. Wilson, M. Winton, A. T. Wittenberg,

B. Wyman, B. Xiang, The GFDL global atmosphere and land model AM4.0/LM4.0: 1. Simulation characteristics with prescribed SSTs. *J. Adv. Model. Earth Syst.* **10**, 691–734 (2018).
16. M. Zhao, J.-C. Golaz, I. M. Held, H. Guo, V. Balaji, R. Benson, J.-H. Chen, X. Chen, L. J. Donner, J. P. Dunne, K. Dunne, J. Durachta, S.-M. Fan, S. M. Freidenreich, S. T. Garner, P. Ginoux, L. M. Harris, L. W. Horowitz, J. P. Krasting, A. R. Langenhorst, Z. Liang, P. Lin, S.-J. Lin, S. L. Malyshev, E. Mason, P. C. D. Milly, Y. Ming, V. Naik, F. Paulot, D. Paynter, P. Phillipps, A. Radhakrishnan, V. Ramaswamy, T. Robinson, D. Schwarzkopf, C. J. Seman, E. Shevliakova, Z. Shen, H. Shin, L. G. Silvers, J. R. Wilson, M. Winton, A. T. Wittenberg, B. Wyman, B. Xiang, The GFDL global atmosphere and land model AM4.0/LM4.0: 2. Model description, sensitivity studies, and tuning strategies. *J. Adv. Model. Earth Syst.* **10**, 735–769 (2018).
17. I. M. Held, B. J. Soden, Robust responses of the hydrological cycle to global warming. *J. Climate* **19**, 5686–5699 (2006).
18. T. Matsuno, Quasi-geostrophic motions in the equatorial area. *J. Meteorol. Soc. Jpn.* **44**, 25–43 (1966).
19. A. E. Gill, Some simple solutions for heat-induced tropical circulation. *Q. J. Roy. Meteorol. Soc.* **106**, 447–462 (1980).
20. M. Wheeler, G. N. Kiladis, Convectively coupled equatorial waves: Analysis of clouds and temperature in the wavenumber–frequency domain. *J. Atmos. Sci.* **56**, 374–399 (1999).
21. G. N. Kiladis, M. C. Wheeler, P. T. Haertel, K. H. Straub, P. E. Roundy, Convectively coupled equatorial waves. *Rev. Geophys.* **47**, 10.1029/2008RG000266 (2009).
22. H. Bartana, C. I. Garfinkel, O. Shamir, J. Rao, Projected future changes in equatorial wave spectrum in CMIP6. *Climate Dynam.* **60**, 3277–3289 (2023).
23. J. Dias, M. Gehne, G. N. Kiladis, N. Sakaeda, P. Bechtold, T. Haiden, Equatorial waves and the skill of NCEP and ECMWF numerical weather prediction systems. *Mon. Weather Rev.* **146**, 1763–1784 (2018).
24. N. J. Weber, D. Kim, C. F. Mass, Convection–Kelvin wave coupling in a global convection-permitting model. *J. Atmos. Sci.* **78**, 1039–1055 (2021).
25. X. Ji, T. Feng, P. Huang, X. Cheng, J. Qin, B. Yang, Evaluation of convectively coupled Kelvin waves in CMIP6 coupled climate models. *Atmos. Res.* **325**, 108214 (2025).
26. M. F. Khairoutdinov, D. A. Randall, Cloud resolving modeling of the ARM summer 1997 IOP: Model formulation, results, uncertainties, and sensitivities. *J. Atmos. Sci.* **60**, 607–625 (2003).
27. Z. Kuang, Weakly forced mock Walker cells. *J. Atmos. Sci.* **69**, 2759–2786 (2012).
28. W. W. Grabowski, J.-I. Yano, M. W. Moncrieff, Cloud resolving modeling of tropical circulations driven by large-scale SST gradients. *J. Atmos. Sci.* **57**, 2022–2040 (2000).
29. Z. Kuang, Modeling the interaction between cumulus convection and linear gravity waves using a limited-domain cloud system–resolving model. *J. Atmos. Sci.* **65**, 576–591 (2008).
30. N. Z. Wong, Z. Kuang, The effect of different implementations of the weak temperature gradient approximation in cloud resolving models. *Geophys. Res. Lett.* **50**, e2023GL104350 (2023).
31. Z. Kuang, A moisture-stratiform instability for convectively coupled waves. *J. Atmos. Sci.* **65**, 834–854 (2008).
32. F. Ahmed, Á. F. Adames, J. D. Neelin, Deep convective adjustment of temperature and moisture. *J. Atmos. Sci.* **77**, 2163–2186 (2020).
33. J. D. Neelin, I. M. Held, Modeling tropical convergence based on the moist static energy budget. *Mon. Weather Rev.* **115**, 3–12 (1987).
34. R. C. Wills, X. J. Levine, T. Schneider, Local energetic constraints on Walker circulation strength. *J. Atmos. Sci.* **74**, 1907–1922 (2017).
35. A. B. Sokol, T. M. Merlis, S. Fueglistaler, No "wet gets wetter" in kilometer-scale mock-Walker circulations. *AGU Adv.* **7**, e2025AV002040 (2026).
36. C. J. Muller, I. M. Held, Detailed investigation of the self-aggregation of convection in cloud-resolving simulations. *J. Atmos. Sci.* **69**, 2551–2565 (2012).
37. A. A. Wing, K. Emanuel, C. E. Holloway, C. Muller, "Convective self-aggregation in numerical simulations: A review" in *Shallow Clouds, Water Vapor, Circulation, and Climate Sensitivity*, R. Pincus, D. Winker, S. Bony, B. Stevens, Eds. (Springer, 2018), pp. 1–25.
38. L. Yao, D. Yang, Convective self-aggregation occurs without radiative feedbacks in warm climates. *Geophys. Res. Lett.* **50**, e2023GL104624 (2023).
39. N. A. Rayner, D. E. Parker, E. B. Horton, C. K. Folland, L. V. Alexander, D. P. Rowell, E. C. Kent, A. Kaplan, Global analyses of sea surface temperature, sea ice, and night marine air temperature since the late nineteenth century. *J. Geophys. Res. Atmos.* **108**, 4407 (2003).
40. W. D. Collins, P. J. Rasch, B. A. Boville, J. J. Hack, J. R. McCaa, D. L. Williamson, B. P. Briegleb, C. M. Bitz, S. J. Lin, M. Zhang, The formulation and atmospheric simulation of the Community Atmosphere Model version 3 (CAM3). *J. Climate* **19**, 2144–2161 (2006).
41. N. J. Lutsko, T. W. Cronin, The transition to double-celled circulations in Mock-Walker simulations. *Geophys. Res. Lett.* **51**, e2024GL108945 (2024).
42. A. A. Wing, K. A. Reed, M. Satoh, B. Stevens, S. Bony, T. Ohno, Radiative–convective equilibrium model intercomparison project. *Geosci. Model Dev.* **11**, 793–813 (2018).
43. H. Quan, Y. Zhang, S. Fueglistaler, Weakening of tropical free-tropospheric temperature gradients with global warming. *J. Atmos. Sci.* **82**, 31–43 (2025).
44. O. Pauluis, S. Garner, Sensitivity of radiative-convective equilibrium simulations to horizontal resolution. *J. Atmos. Sci.* **63**, 1910–1923 (2006).
45. D. J. Raymond, S. L. Sessions, A. H. Sobel, Ž. Fuchs, The mechanics of gross moist stability. *J. Adv. Model. Earth Syst.* **1**, 10.3894/JAMES.2009.1.9 (2009).
46. J.-Y. Yu, C. Chou, J. D. Neelin, Estimating the gross moist stability of the tropical atmosphere. *J. Atmos. Sci.* **55**, 1354–1372 (1998).

Acknowledgments: We gratefully acknowledge M. F. Khairoutdinov for creating and maintaining SAM and Z. Kuang for developing the damped gravity wave method that couples SAM to large-scale gravity waves. We gratefully acknowledge N. Wong and Q. Song for making the source code of the damped gravity wave method for SAM publicly available and for technical support. The authors acknowledge T. Merlis, N. Jeevanjee, and D. Yang for helpful discussions. We acknowledge three reviewers for helpful comments. **Funding:** This report was prepared by H.Q. under Award NA23OAR4320198-T1-01 from the National Oceanic and Atmospheric Administration, U.S. Department of Commerce. H.Q. is the recipient of the funding. The statements, findings, conclusions, and recommendations are those of the author(s) and do not necessarily reflect the views of the National Oceanic and Atmospheric Administration, or the U.S. Department of Commerce. **Author contributions:** Conceptualization: H.Q., Y.Z., G.D., and S.F. Methodology: H.Q., Y.Z., G.D., and S.F. Software: H.Q. Investigation: H.Q. Formal analysis: H.Q. and G.D. Validation: H.Q. Data curation: H.Q. Visualization: H.Q. Supervision: Y.Z. and S.F. Writing—original draft: H.Q. and S.F. Writing—review and editing: H.Q., Y.Z., and G.D. Resources: H.Q. and S.F. Project administration: Y.Z. Funding acquisition: S.F. **Competing interests:** The authors declare that they have no competing interests. **Data, code, and materials availability:** All data and code needed to evaluate and reproduce the results in the paper are present in the paper and/or the Supplementary Materials. This study did not generate any new materials. Postprocessed model output and plotting scripts can be found at https://datacommons.princeton.edu/discovery/catalog/doi-10-34770-8s66-k619. The source code for SAM can be found at http://rossby.msrc.sunysb.edu/SAM.html. The source code for SAM coupled to large-scale gravity waves can be found at https://github.com/KuangLab-Harvard/SAM_SRCv6.11. The source code for GFDL-AM4 can be found at https://zenodo.org/records/1199643.

Submitted 16 October 2025
Accepted 2 June 2026
Published 7 August 2026
10.1126/sciadv.aed1634

Science Advances

Periodic extreme rainfall in a warmer climate due to stronger convectively coupled waves

Heng Quan, Yi Zhang, Guy Dagan, and Stephan Fueglistaler

Sci. Adv. **12** (32), eaed1634. DOI: 10.1126/sciadv.aed1634

Science Advances (ISSN 2375-2548) is published by the American Association for the Advancement of Science. 1200 New York Avenue NW, Washington, DC 20005. The title *Science Advances* is a registered trademark of AAAS.